# Integrated Study of the Calcination Cycle from Gibbsite to Corundum

Matthew R. Hill,[†] Timothy J. Bastow,[†,‡] Steven Celotto,[§] and Anita J. Hill*[,†,||]

*CSIRO Manufacturing and Materials Technology, Private Bag 33, South Clayton MDC, Victoria 3169, Australia, School of Chemistry and Department of Materials Engineering, Monash University, Clayton, Victoria 3800, Australia, and Innovative Manufacturing Research Centre, Engineering Department, Cambridge University, Unit 26a Cambridge Science Park, Cambridge CB4 0FP, United Kingdom*

*Received January 9, 2007. Revised Manuscript Received February 28, 2007*

A comprehensive picture of the gibbsite ($Al(OH)_3$) to corundum ($\alpha$-$Al_2O_3$) calcination process has been developed by multi-technique characterization of an integrated sample set. In 100 °C calcination stages, $^{27}Al$ nuclear magnetic resonance (NMR), differential thermal analysis (DTA), X-ray diffraction (XRD), and nitrogen sorption surface area measurements were employed to elucidate the structure and chemistry of these calcinates. In addition, positron annihilation lifetime spectroscopy (PALS) has been used to study the defective nature of these aluminas. By exploiting the complementarity of PALS, $^{27}Al$ NMR, and $N_2$ sorption, new links were established between particle morphology, local atomic coordination, and surface defect chemistry.

## Introduction

Gibbsite ($Al(OH)_3$) is an important aluminum ore, being one of the three materials that comprise bauxite. It is a structural precursor to corundum ($\alpha$-$Al_2O_3$), with the mica-like layout of $Al^{3+}$ ions within the gibbsite sheets essentially acting as a "floor plan" for the formation of three-dimensional corundum networks upon heating. The intermediate products, the transition aluminas, and in particular $\gamma$-alumina have been the subject of much study because of their use as catalyst supports.[1] It is believed that most important structural and textural properties of subsequent aluminas produced downstream are strongly influenced by similar factors in the parent gibbsite.[2] However, it is also clear that the method of heat treatment can strongly affect the nature of the calcinates produced, indicating that the products of the calcination process are dependent on a range of parameters. The work in this field has been previously summarized.[3,4] Most experimental reports involve the use of different techniques on separate sample sets, meaning that there are currently some unclear results leading to contradictory statements. The differences appear to depend upon the nature of the seed gibbsite samples initially employed for these studies.

The principal analytical tools in these previous studies have been X-ray and electron diffraction. More recently a number of reports of high field $^{27}Al$ MAS (magic angle spinning) NMR have appeared on the topic of the calcination stages of aluminum hydrates.[5−9] In such studies the $^{27}Al$ NMR spectrum yields via the chemical shifts, a characteristic signature of the aluminum hydroxide/oxide phases present and also provides a means of determining the concentration of the various $AlO_n$ oxygen coordination configurations by straightforward line-shape integration. $^{27}Al$ NMR has been found to be a good means of detecting the onset of phase changes following calcination, because long range order is not a prerequisite for the NMR fingerprint.

Independently of the NMR work, there have been some reports of the use of positron annihilation lifetime spectroscopy (PALS) to probe the surface and defect structure of alumina powders, films, and interfaces.[10−14] PALS is a powerful technique capable of characterizing free volume in solids on a scale ranging from atomic vacancies (subna-

* To whom corresondence should be addressed. E-mail: anita.hill@csiro.au.
[†] CSIRO Manufacturing and Materials Technology.
[‡] Department of Materials Engineering, Monash University.
[§] Cambridge University .
[||] School of Chemistry, Monash University.

(1) Brunelle, J. P.; Nortier, P.; Poisson, R. In *Catalysts and Supports Catalysts*; Stiles, A. B., Ed.; Butterworth: Boston, 1987; pp 11−55.
(2) Raybaud, P.; Digne, M.; Iftimie, R.; Wellens, W.; Euzen, P.; Toulhoat, H. *J. Catal.* **2001**, *201*, 236.
(3) Wefers, K.; Misra, C. Alcoa Technical Paper No. 19, Revised; Alcoa Labs: 1987.
(4) Euzen, P.; Raybaud, P.; Krokidis, X.; Toulhoat, H.; Le Loarer, J.-L.; Jolivet, J.-P.; Froidefond, C. In *Handbook of Porous Materials*; Schüth, F., Sing, K., Weitkamp, J., Eds.; Wiley-VCH: Weinheim, Germany, 2002; Chapter 4.7.2, pp 1591−1677.
(5) Slade, R. C. T.; Southern, J. C.; Thompson, I. M. *J. Mater. Chem.* **1991**, *1*, 563.
(6) Slade, R. C. T.; Southern, J. C.; Thompson, I. M. *J. Mater. Chem.* **1991**, *1*, 875.
(7) Bastow, T. J.; Hall, J. S.; Smith, M. E. *Flash Reaction Processes*; Davies, T. W., Ed.; Kluwer Academic Publishers: Norwell, MA, 1995; p 123.
(8) Bastow, T. J.; Smith, M. E.; Hall, J. S.; Steuernagel, S. *Mater. Lett.* **1994**, *18*, 197.
(9) Meinhold, R. H.; Slade, R. C. T.; Newman, R. H. *Appl. Magn. Reson.* **1993**, *4*, 121.
(10) Brauer, G.; Kerbe, F.; Kajcsos, Z.; Ashry, A. *Phys. Status Solidi A* **1984**, *84*, 451.
(11) Schaeffer, H. E.; Forster, M. *Mater. Sci. Eng.* **1989**, *A109*, 161.
(12) Hasegawa, M.; Tabata, M.; Miyamoto, T.; Nahashima, Y.; Hyodo, T.; Fujinami, M.; Yamaguchi, S. *Mater. Sci. Forum* **1995**, *175−178*, 269.
(13) Xu, J.; Somieski, B.; Hulett, L. D.; Pint, B. A.; Tortorelli, P. F. *Appl. Phys. Lett.* **1997**, *71*, 3165.
(14) Xu, J.; Hulett, L. D.; Somieski, B.; Suzuki, R.; Ohdaira, T. *Mater. Sci. Forum* **1997**, *255−257*, 214.

10.1021/cm070078f CCC: $37.00 
Published on Web 04/28/2007

nometer) to mesopores (several nanometers).[15] These studies have revealed vacancy-type defects in the alumina powders including mono- and di-vacancies, vacancy clusters, and microvoids. However, the size and prevalence of these defects has been found to vary strongly according to the method by which the aluminas were prepared. As far as we are aware, there have been no reports on the use of PALS to study the numerous intermediates in the complete calcination cycle from gibbsite to corundum.

As mentioned above, there are discrepancies in characterization results across the reports in the field, presumably as a result of variations in the seed gibbsites employed. Differences include the reported thermal properties[4,16−18] where transitions were not always observed, and the temperatures at which they occurred also varied. The transition temperatures between the phases as indicated by X-ray diffraction (XRD) have been seen to differ by hundreds of degrees.[4,17−19] For example, the onset of the terminal $\alpha$-$Al_2O_3$ phase has been found to range between 700 °C[17] and 1350 °C.[16] Significant differences in the $AlO_4$ content from $^{27}$Al MAS NMR at various calcination temperatures have also been reported.[9,16,18] Theoretical studies of the calcination process have further highlighted the role of the gibbsite precursor structure in the nature of subsequent calcines such as $\gamma$-$Al_2O_3$ through a mechanism of hydrogen transfer and water extraction.[20] The role of the potential experimental conditions upon the structure of the product was also shown to be significant.[2]

The present investigation combines both $^{27}$Al MAS NMR and PALS, in conjunction with XRD and surface area (BET) measurements, to determine the crystallographic and physical state of 12 specimens of $Al(OH)_3$ gibbsite heated from 100 °C to 1200 °C in 100 °C steps and then cooled to room temperature for examination. This work presents an integrated approach to the characterization of the alumina species between gibbsite and corundum via a number of techniques using the same specimens.

## Experimental Section

Seed gibbsite ($Al(OH)_3$; $D_{50}$ 98.7 $\mu$m, standard deviation 38.9 $\mu$m) was obtained from Alcoa of Australia Limited and was used as received. The set of samples for this study was prepared by soak calcination in flowing air for 2 h across the range of 100−1200 °C at 100 °C increments.

The NMR measurements were made with a Bruker Avance 400 spectrometer in a nominal field of 9.4 T. The $^{27}$Al spectra were observed using an MAS probe with 2.5 mm PSZ rotors and a rotation frequency of approximately 20 kHz. The excitation pulse length was 1 $\mu$s, and the pulse repetition time was 2 s. The spectra were referenced with respect to the $AlO_6$ peak in $Y_3Al_5O_{12}$ (YAG) at +0.7 ppm. Because the $AlO_6$ and $AlO_4$ lineshapes were asymmetric (due to a dispersion of $^{27}$Al nuclear quadrupole coupling constants) and outside the Gaussian−Lorentzian mix provided by standard fitting programs, an arbitrary division between the $AlO_6$ and $AlO_4$ regions was made by integrating down-frequency and up-frequency from a point at the minimum near 30 ppm in the total line shape.

The source for the PALS experiments was made using aqueous $^{22}$NaCl, with an activity of about 20 $\mu$Ci, which was evaporated onto a 2.5 $\mu$m thick annealed Ti foil (0.114 mg cm$^{-2}$) and covered by a second foil. The resulting foil sandwich was crimp sealed. The lifetime experiments were made using a fast−fast coincidence spectrometer. The equipment was thermally stabilized at 22.5 ± 0.5 °C. The fast coincidence cutoff was set to 50 ns. The resolution function measured using$^{22}$ NaCl had a full width at half-maximum value of 250 ps. The positron lifetime spectra contained about $1 \times 10^6$ counts. The spectra were evaluated using the program PFPOSFIT[21] to fit the data as the sum of decaying exponentials. The source component was detected using polished aluminum standards which gave repeatable spectra of $\tau_1 = 166 \pm 1$ ps (intensity $I_1 = 98 \pm 0.5\%$) attributed to the Al and $\tau_2 = 450 \pm 35$ ps ($I_2 = 2 \pm 0.5\%$) attributed to the NaCl. Hence a source correction of $\tau_2 = 450$ ps and $I_2 = 2\%$ for annihilations taking place in the NaCl was used in the data analysis. Powder specimens of 2 mm thickness were compacted into aluminum pans 1 cm in diameter, and the 2 mm spot source foil was sandwiched between the powder specimens. Experiments were performed in air.

Powder XRD spectra were collected on a Siemens X-ray diffractometer with a Cu K$\alpha$ source ($\lambda = 1.5418$ Å) for $2\theta$ values from 25° to 75°. BET surface area measurements were made under pure $N_2$ in a Micromeritics ASAP 2000 analyzer using 0.5 g of sample with a drying temperature for all specimens of 300 °C (except for the 100 °C and 200 °C samples which were dried at their calcination temperatures). A working pressure of 805 mm of Hg was used, and at least six points were acquired to make the surface area measurement. If the data did not fit a straight line to a correlation of at least 0.98, the experiment was repeated. The differential thermal analysis/therogravimetric (DTA/TG) measurements were made in an open pan with a heating rate of 10 °C min$^{-1}$ under an air atmosphere with a flow rate of 20 mL min$^{-1}$ on a Stanton Redcroft STA 1500 simultaneous TGA/DTA analyzer.

## Results and Discussion

The XRD data for the calcined aluminas are shown in Figure 1. The 100 °C calcination steps indicate the successive phase transitions from gibbsite to corundum, as compared to the more limited scope of previous XRD work.[22−24] By comparing observed diffraction peaks to reference patterns, the temperatures for the emergence of various crystalline phases have been determined with XRD. The transition from gibbsite to highly crystalline boehmite is sharply defined at 300 °C. At this point a $\chi$-alumina component is also faintly detectable in XRD patterns, becoming more prominent at the next calcination step. Bearing in mind the 100 °C calcination steps, at 500 °C a clear transition to the disordered spinel $\gamma$-alumina phase is evident. Further development of

(15) Schmidt, W. Positron annihilation spectroscopy. In *Handbook of Porous Solids*; Schüth, F., Sing, K. S. W., Weitkamp, J., Eds.; Wiley-VCH: Heidelberg, 2002; pp 506−532.
(16) MacKenzie, K. J. D; Temuujin, J.; Okada, K. *Thermochim. Acta* **1999**, *327*, 103.
(17) Kano, J.; Saeki, S; Saito, M; Yamazaki, S. *Int. J. Miner. Process.* **2000**, *60*, 91.
(18) Ingram-Jones, V. J.; Slade, R. C. T.; Davies, T. W.; Southern, J.C.; Salvador, S. *J. Mater. Chem.* **1996**, *6* (1), 73.
(19) Bokhimi, X.; Toledo-Antonio, J. A.; Guzman-Castillo, M. L.; Mar-Mar, B.; Hernandez-Beltran, F.; Navarrete, J. *J. Solid State Chem.* **2001**, *161*, 319.
(20) Krokidis, X.; Raybaud, P.; Gobichon, A. E.; Rebours, B.; Euzen, P.; Toulhoat, H. *J. Phys. Chem. B* **2001**, *105*, 5121.
(21) Puff, W. *Comput. Phys. Commun.* **1983**, *30*, 359.
(22) Fredrickson, L. D. *Anal. Chem.* **1954**, *26*, 1883.
(23) Kolesova, V. A. *Opt. Spektrosk.* **1959**, *6*, 20.
(24) Cabannes-Ott, C. C. R. *Acad. Sci.* **1957**, *244*, 2491.

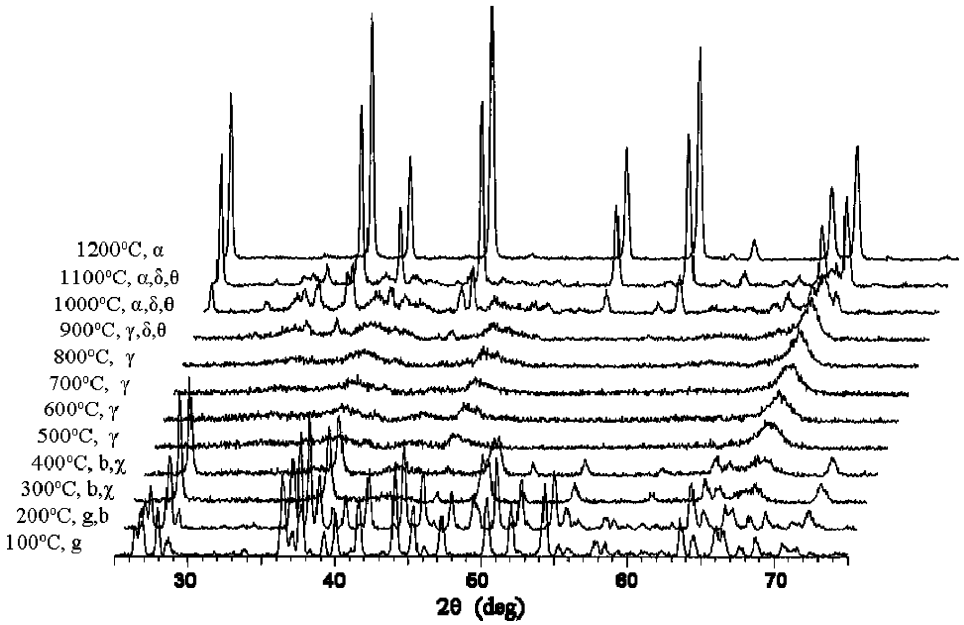


**Figure 1.** XRD stackplot showing the phase transitions with increasing calcination temperature. Phases were assigned by comparison to reference patterns.

more ordered transition aluminas, the $\delta$- and $\theta$-phases, becomes clear above 900 °C, before the final evolution of α-alumina (corundum) which commences at 1000 °C and becomes fully established by 1200 °C.

A DTA/TG plot for seed gibbsite heated from 100 to 1200 °C is displayed in Figure 2. The DTA component exhibits three endothermic phase change events at 247.0 °C, 319.4 °C, and 528.5 °C. The first two events are associated with the loss of water during the transformation from gibbsite to boehmite, and the latter with a further transition from boehmite to $\gamma$-$Al_2O_3$. The endotherms are accompanied by an overall weight loss of 32.8%, which is in reasonable agreement with the expected value of 34.6% for the overall transition from $Al(OH)_3$ to $Al_2O_3$. The shoulder at 247.0 °C has been previously reported[16,19] to be due to evolved water from particle surfaces during the transition from gibbsite to boehmite. When smaller particles have been investigated, this feature has not been as prevalent in DTA spectra.[3] Particle sizing of the gibbsite used for the present study revealed a $D_{50}$ of 98.7 $\mu$m. Clearly, there is an increase in the energy required for water to escape from within the bulk of large (some particles of 200 $\mu$m observed) particles when compared to that released from the surface (endotherms observed at 319.4 °C and 247.0 °C respectively). Higher temperature transitions between the various phases of $Al_2O_3$ were not observed; the energy associated with such changes was presumably too small to be detected in these scans. The sensitivity of DTA in these experiments was limited by the need for an open pan to allow the release of evolved water during the calcination. Closed pan experiments revealed wide variations in observed transition temperatures as a result of the buildup of pressure within the system associated with the evolution of water vapor.

The $^{27}$Al MAS NMR spectra for $Al(OH)_3$ gibbsite specimens annealed at 100 °C intervals are shown in Figure 3. The gibbsite structure contains two distinct octahedrally coordinated ($AlO_6$) Al sites per unit cell. An analysis of the gibbsite $^{27}$Al line shape, giving its decomposition into two lines (one with second-order quadrupolar structure) is given in ref 6. Despite the fact that the crystal structure of boehmite contains only one octahedrally coordinated aluminum site, the $^{27}$Al spectra at 300 °C and 400 °C indicate a 10−12% $AlO_4$ content. The next phase transition according to XRD is $\chi$-alumina; however, the structures proposed by Saalfeld and Wedde[25] and Brindley and Choe[26] for $\chi$-alumina also contain only $AlO_6$. The transition to boehmite (AlOOH) from gibbsite ($Al(OH)_3$) can be violent for gibbsite particles of the size used here, when rapidly heated, because of buildup of pressure and subsequent energetic decomposition of the crystallites as the water is expelled.[4,27] This unusual coordination chemistry correlates well with the DTA spectrum shown in Figure 2, where two endotherms associated with the expulsion of water were observed as a result of the significant difference in environments between surface and bulk species. The $AlO_4$ sites could therefore occur as a result of the disordered nature of the boehmite framework, shattered by rapid water expulsion, on which the crystallites form.

The $\gamma$-$Al_2O_3$ phase (ca. 500−900 °C) has been assigned[28] a spinel lattice $AB_2O_4$ in which all the octahedral $BO_6$ sites are filled with Al atoms and the remaining Al fill only 2/3 of the tetrahedral $AO_4$ sites, leaving 1/3 of the A sites vacant, that is, $Al_{2/3}\square_{1/3}Al_2O_4$, which satisfies charge neutrality. This assignment is satisfactorily confirmed by measuring the integrated intensity of the $AlO_4$ and $AlO_6$ lines (with maxima at 65 and 10 ppm shift, respectively) of the $^{27}$Al NMR spectrum. The asymmetric lineshapes are a consequence of the atomic disorder due to the random assignment of the vacancies within the 1/3 vacancy component of the tetrahedral metal sites in the spinel lattice. The percentage of the $AlO_4$ content as a function of temperature is displayed in Figure 4. At 700 °C, in the middle of the $\gamma$-phase temperature

(25) Saalfeld, H.; Wedde, M. *Z. Kristallogr.* **1974**, *139* (1−2), 129.
(26) Brindley, G. W.; Choe, J. O. *Am. Mineral.* **1961**, *46*, 771.
(27) DeBoer, J. H.; Fortuin, J. M. H.; Steggerda, J. J. *Proc. K. Ned. Akad. Wet.* **1954**, *57*, 434.
(28) Lippens, B. C.; DeBoer, J. H. *Acta Crystallogr.* **1964**, *17*, 1312.

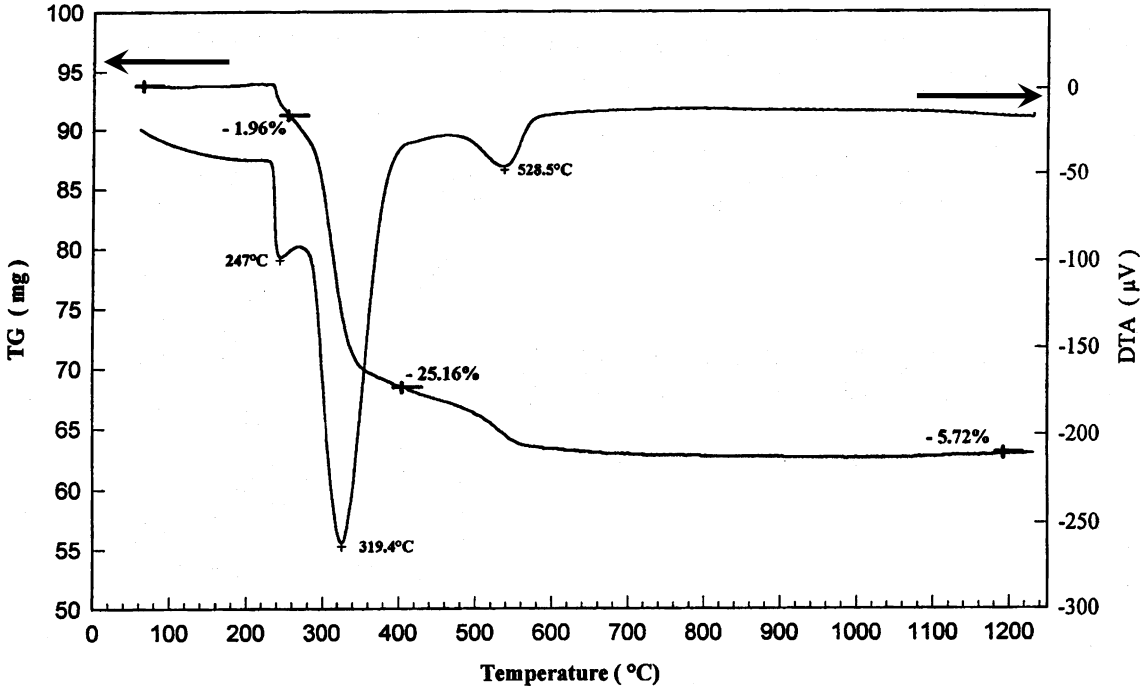


**Figure 2.** Simultaneous DTA/TG showing endothermic phase transitions associated with stepwise dehydration for the series gibbsite, boehmite, $\gamma$-$Al_2O_3$.

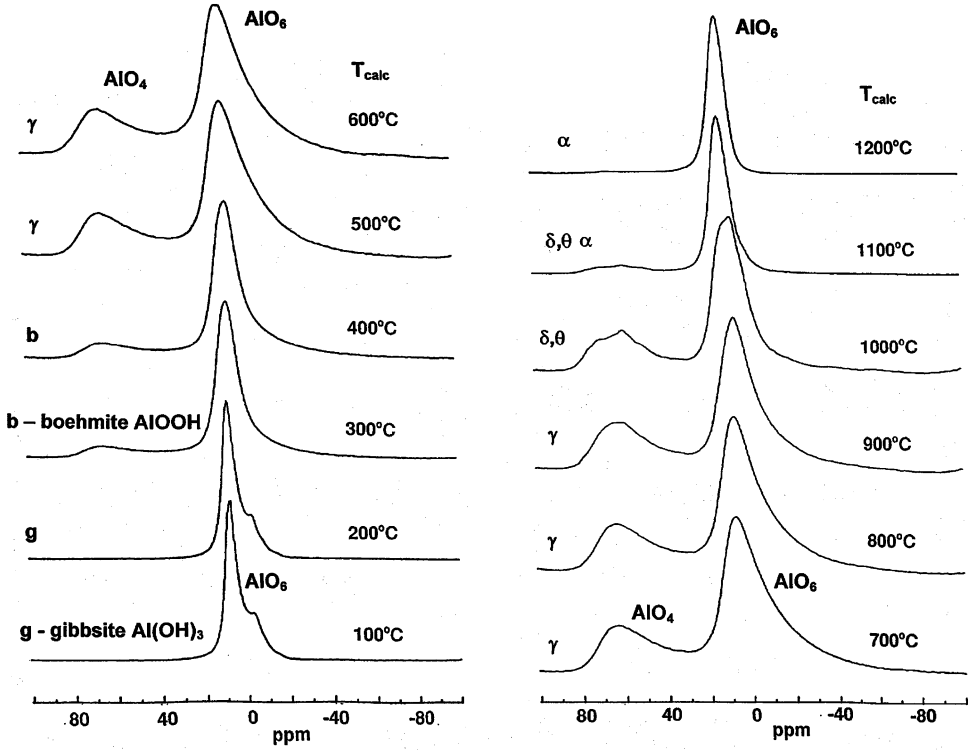


**Figure 3.** Stackplot of $^{27}$Al NMR spectra showing the relative phase variation in local coordination environment with respect to the calcination steps employed.

range, the $AlO_4$ content is very close to 25% as required by the model.[29,30] Above this temperature, the proportion of tetrahedral sites increases. Presumably, this increase is due to the emergence of small amounts of $\delta$-$Al_2O_3$, which is known to possess a unit cell structure that can be described as a triple block of spinels,[31,32] which would account for the proportional increase of filled Al tetrahedral sites. While the actual values differ, there is a close match in the overall trend of site occupancies to that previously reported.[16] For $T_{calc}$ = 900−1000 °C there is spectroscopic evidence for further transition aluminas, presumably the $\delta$ and $\theta$ phases. The $AlO_4$ content starts to decrease at this temperature (Figure 4), with the resonance showing signs of structural rearrangement as a result of transition to the final $\alpha$-$Al_2O_3$ which

(29) John, C. S.; Alma, N. C. M.; Hays, G. R. *Appl. Catal.* **1983**, *6*, 341.
(30) Dupree, R.; Farnan, I. E.; Forty, A. J.; El-Mashri, S.; Bottyan, L. *J. Phys., Colloq.* **1985**, *C8*, 113.
(31) Lippens, B. C. Ph.D. Thesis, Technical University Delft, Delft, 1961.
(32) Saalfeld, H.; Mehotra, B. B. *Naturwissenschaften* **1966**, *53*, 128.

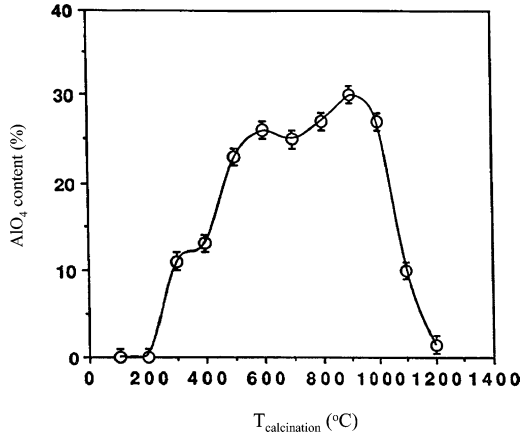


**Figure 4.** Plot of % $AlO_4$ content in $^{27}Al$ NMR spectra as a function of calcination temperature.

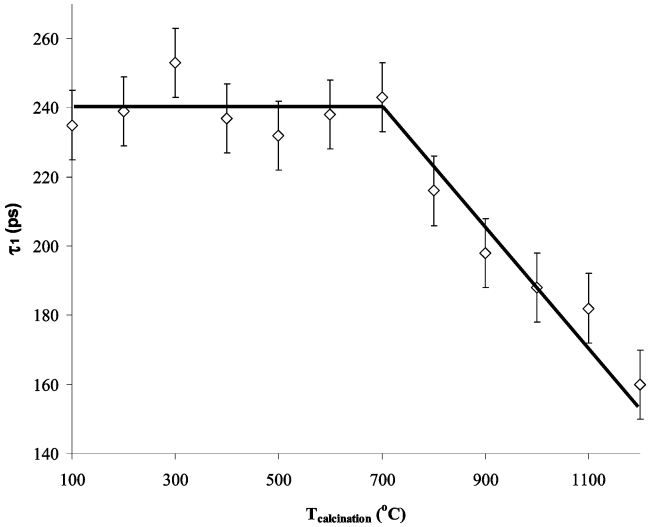


**Figure 5.** $\tau_1$ lifetime component in PALS spectra of the alumina calcinates. Trendlines are included as a guide only.

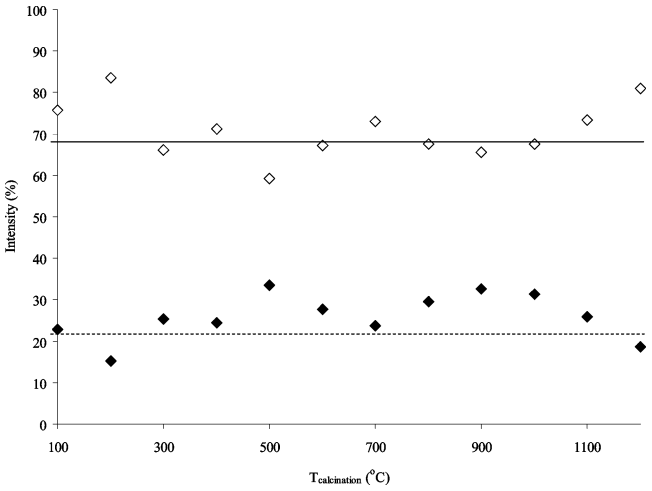


**Figure 6.** Annihilation intensities of lifetime components $\tau_1$ and $\tau_2$. Trendlines are included as a guide only.

contains only $AlO_6$ sites. At 1100 °C and 1200 °C the α-phase is dominant. The appearance of this phase coincides with a sharp drop off in the relative number of $AlO_4$ sites present within the structure as the well-defined hexagonal corundum forms, containing a single $AlO_6$ site.

At no stage in our soak calcination sequence was $AlO_5$ observed, in contrast to aluminas prepared by flash calcination[18,33] or vacuum dehydration.[6] Because the presence of $AlO_5$ is regarded as an indicator of disorder and is also regarded as a surface active site, control of its presence or absence by experimental means is significant.

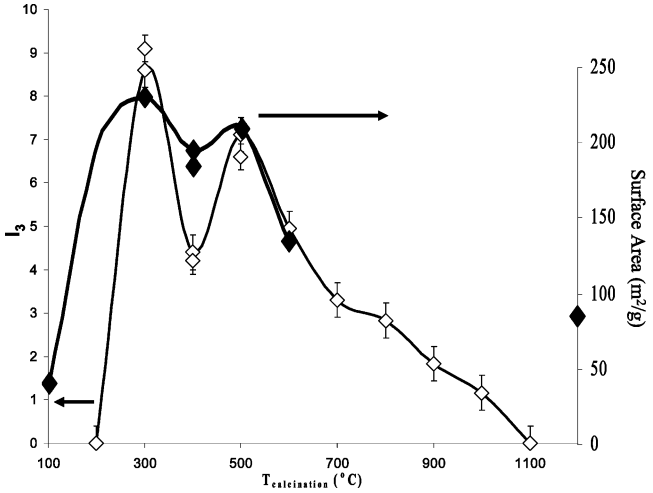


**Figure 7.** Simultaneous plots of *ortho*-positronium intensity, $I_3$, and BET surface area, showing a close relationship.

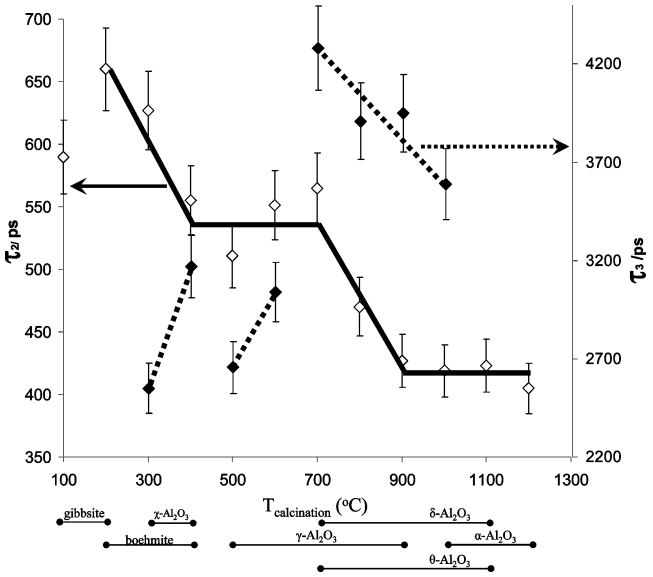


**Figure 8.** Longer PALS lifetime components $\tau_2$ and $\tau_3$ as functions of calcination temperature. Assigned phases from XRD and NMR have been included for clarity. Trendlines are included as a guide only.

Previous PALS studies of variously prepared aluminas[10−14,40] have shown three distinct lifetime components: (1) $e^+$ trapped in vacancies, $\tau_1 = 160-300$ ps; (2) $e^+$ trapped in extended lattice defects, $\tau_2 = 400-700$ ps; and (3) *ortho*-positronium ($e^+e^-$) at surfaces, $\tau_3 > 1$ ns.

The present PALS results are shown in Figures 5−8. PALS provides a link between analyses that give information on short-range atomic order (NMR) and those that shed light upon larger scale structure (XRD, BET, DTA). PALS can quantify free volume elements in a size range from mono-vacancies to mesoporosity in solids. The lifetime of the positron, prior to annihilation with an electron, is longer when it is localized in areas of lower electron density, such as

(33) Kunath-Fandrei, G.; Bastow, T. J.; Hall, J. S.; Jäger C.; Smith, M. E. *J. Phys. Chem.* **1995**, *99*, 15138.

vacancies and pores, with the intensity of each component indicating the concentration of defects. The size of internal and external pores can be reliably determined from the *ortho*-positronium lifetime *via* the application of an extension[34] to the original Tao-Eldrup model. We have recently demonstrated the applicability of the technique to highly porous materials, similar in structure to those of the present investigation.[35]

Figure 5 is a plot of positron lifetime $\tau_1$ versus calcination temperature and gives an indication of the nature of atomic vacancies throughout the crystal lattice as a function of temperature. Below 700 °C the positron lifetime $\tau_1$ is essentially constant at approximately 240 ps, indicative of a state with positrons trapped in structural vacancies in disordered aluminas.[11] Above 700 °C there is a steady decrease in the observed lifetime to 165 ps, in accordance with a linear combination of lifetimes for two vacancy types. The 165 ps state is attributed to positrons trapped in monovacancies in $\alpha$-$Al_2O_3$.[12,14] As mentioned above, this transition is associated with the change from the spinel $\gamma$-$Al_2O_3$, in which 1/3 of tetrahedral sites are vacant through to the completely octahedral end product corundum.[13] We did not detect a free positron state ($\tau_0 = 70$ ps)[11,13] in these aluminas so that the $\tau_1$ values measured here indicate "saturation" at vacancy defects where the specific positron trapping rate in a saturated state is of the order of $4 \times 10^{14}$ $s^{-1}$.[36] From our results we can estimate a lower limit for atomic vacancy concentration in all of these aluminas, including highly ordered $\alpha$-$Al_2O_3$, of at least 100 ppm.[37,38]

The values measured for $\tau_2$ ranged from 650 ps to 400 ps decreasing in stages with respect to increasing calcination temperature. We attribute $\tau_2$ to the trapping of positrons in defect layers or extended lattice defects similar to that found by Brauer et al.[10,40] and Schaefer and Forster[11] The *ortho*-positronium component, $\tau_3$, ranged from 2.4 ns to 4.3 ns and is attributed to an *ortho*-positronium surface state similar to that reported by Xu et al.[13,14] in aluminas and Boskovic et al.[35] in mesoporous silicas.

Figure 6 is a plot of relative intensities for lifetime components $\tau_1$ and $\tau_2$. Within the levels of expected variation, there are no clear trends for any changes in the number of positrons trapped in vacancies ($I_1$) or lattice defect layers ($I_2$). The features that arise from Figure 7, an overlay of plots for *ortho*-positronium surface state intensity, $I_3$, and BET surface area, are much more striking. The fact that the positron results closely match the plotted surface areas indicate that *ortho*-positronium dominantly favors annihilation at surface features and also that all pores in the materials must be connected to the surface, as they are accessible by nitrogen during adsorption measurements. There are two notable peaks in both the BET and the PALS results at both 300 and 500 °C. The surface area values recorded here indicate the formation of an open, macroporous structure, in agreement with previous findings.[3] Dehydration of gibbsite to form boehmite at 300 °C results in a sixfold increase in surface area, due to a mass loss during dehydration that is not accompanied by a related decrease in the external dimensions of the hydroxide particles.[28,39] Following an amount of ordering and removal of surface defects at 400 °C that is linked to a drop in both $I_3$ and surface area, a similar dehydration process gives rise to the peaks at 500 °C, in line with the formation of $\gamma$-$Al_2O_3$ from AlOOH. At higher temperatures the observed surface area plateaus to 85 $m^2$ $g^{-1}$ and the *ortho*-positronium surface contribution tails off to insignificant amounts. This reduction is indicative of the annealing out of surface defects at elevated temperatures. The alumina particles at this stage undergo sintering to form a network of interconnected pores and crystallites that deliver an intrinsic BET surface area of 85 $m^2$ $g^{-1}$.

Figure 8 shows the longer lifetime components $\tau_2$ and $\tau_3$, in which there are a number of distinct features present. The $\tau_2$ component exhibits a monotonic decline from 650 to 400 ps, becoming smaller in stages, with increasing calcination temperature. Presumably the longer lifetimes observed at lower temperatures are due to extended lattice defects intrinsic to gibbsite and boehmite. The decrease in $\tau_2$ with calcination temperature is due to positron trapping at defects with correspondingly higher electron density. This increase in electron density at the trapping site is consistent with the accompanying increase in density of the sequence of alumina phases formed (gibbsite, 2.42 g $cm^{-3}$; boehmite, 3.01 g $cm^{-3}$; $\gamma$-alumina, 3.2 g $cm^{-3}$; $\alpha$-$Al_2O_3$, 3.98 g $cm^{-3}$).[3]

The $\tau_3$ lifetimes (associated with the annihilation of *ortho*-positronium) reveal information on the pore surface structure and chemistry of the aluminas. There are three separate trends in these *ortho*-positronium lifetimes. The $\tau_3$ values show 15−20% increases from 300 to 400 °C (boehmite) and 500−600 °C ($\gamma$-alumina). When these phases initially form at 300 °C and 500 °C, respectively, there are likely to be a number of pores being created as a result of escape of water from the bulk, common to the formation of both boehmite (300 °C) and $\gamma$-alumina (500 °C). When heated a further 100 °C (400 °C, 600 °C), surface pore defects may be annealed out, thereby increasing the mean lifetime and reducing the number of pores and hence the surface area (see Figure 7).

From 600 °C to 700 °C there is a 50% increase in the $\tau_3$ component from 3 to 4.3 ns. There is no destabilizing water evolution from the bulk in this instance (cf. Figure 2). We attribute this increase in *ortho*-positronium lifetime to the development of a sintered network of interconnected pores at 700 °C that gradually reduce in size as the calcination temperature is increased. An *ortho*-positronium lifetime of 4.3 ns corresponds to a mean micropore diameter of 8.8 Å.[35] Calcination at 1100 °C resulted in the elimination of a $\tau_3$

(34) Dull, T. L.; Frieze, W. E.; Gidley, D. W.; Sun, J. N.; Yee, A. F. *J. Phys. Chem. B* **2001**, *105*, 4657.
(35) Boskovic, S.; Hill, A. J.; Turney, T. W.; Gee, M. L.; Stevens, G. W.; O'Connor, A. J. *Prog. Solid State Chem.* **2006**, *34*, 67.
(36) Schaefer, H. E. *Phys. Status Solidi A* **1987**, *102*, 47.
(37) Nieminen, R. M.; Mannineen, M. *Positrons in Solids*; Springer: Berlin, 1979.
(38) Baier, F.; Müller, M. A.; Grushko, B.; Schaefer, H. E. *Mater. Sci. Eng.* **2000**, *294−296*, 650.
(39) Wefers, K. *Erzmetall* **1962**, *15*, 339.
(40) Brauer, G.; Kerbe, F.; Kajcsos, Z.; Ashry, A. *Phys. Status Solidi A* **1984**, *82*, 143.

component as a highly ordered corundum evolved. At this point the surface area of the network is not high enough (~85 $m^2\ g^{-1}$) for formation of a detectable (>1%) *ortho*-positronium surface component.

## Conclusions

Systematic use of a number of characterization techniques probing different length scales has resulted in new insights on the structure and properties of gibbsite calcines. XRD defines the long range ordering characteristics of the phases while NMR gives the amounts of the local $AlO_4$ and $AlO_6$ coordinations. Note that at no stage in the annealing of the cation disordered $\gamma$-$Al_2O_3$ was an $AlO_5$ signal (the hallmark of extreme alumina disorder) observed. Striking changes in the lattice defects and pore surface chemistry were observed by PALS and related closely to corresponding structural and chemical transitions. A correlation between the BET surface area measurements and relative *ortho*-positronium intensity was displayed, providing an insight into pore connectivity and the overall macroporosity of the particles throughout the calcination series. Surface defects, similar to micropores, were detected by PALS, with changes in observed lifetimes being linked to the coalescence of pores during lower temperature water-evolving structural transitions and the consolidation of the pore network during particle sintering at higher temperatures. Stark changes in observed PALS intensity and lifetime components also served to highlight the sensitivity of the technique in indicating these transitions.

It is hoped that the new information provided by this detailed study will be useful in the optimization of existing alumina and aluminum production processes but that the information will also prove valuable in the development of new low-energy electrowinning technologies, such as aluminum deposition in ionic liquids,[41] and in the production of high surface area hierarchically porous metal oxides for use in catalysis, sensors, and energy storage devices.

**Acknowledgment.** We thank Mark Smith, Terry Turney, and David Hay for helpful discussions, Natasha Wright and Mike Goss for experimental assistance, and Barry Robson of Alcoa Australia Pty. Ltd. for samples. We gratefully acknowledge the CSIRO emerging science initiative scheme for funding this work.

CM070078F

(41) Lu, J. M.; Dreisinger, D. *ACS Symp. Ser.* **2003**, *856*, 495.